

# Synergetic Effects of Dual Electrocatalysts for High-Performance Solar-Driven Water Oxidation

Rajender Boddula,<sup>†,||</sup> Beidou Guo,<sup>†,‡,||</sup> Akbar Ali,<sup>†,‡,||</sup> Guancai Xie,<sup>†,‡</sup> Yawen Dai,<sup>†,‡</sup> Chang Zhao,<sup>†,‡</sup> Yuxuan Wei,<sup>†,‡</sup> Saad Ullah Jan,<sup>†,‡</sup> and Jian Ru Gong<sup>\*,†,‡,||</sup>

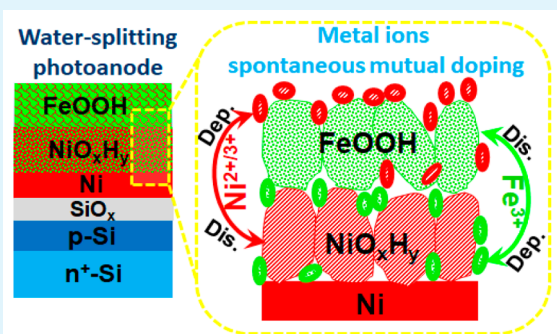
<sup>†</sup>Chinese Academy of Sciences (CAS) Center for Excellence in Nanoscience, CAS Key Laboratory of Nanosystem and Hierarchy Fabrication, National Center for Nanoscience and Technology, Beijing 100190, China

<sup>‡</sup>University of CAS, Beijing 100049, China

## Supporting Information

**ABSTRACT:** Integration of electrocatalysts (ECs) with photoabsorbers is indispensable for high-performance solar water splitting. However, how the interaction between different ECs affects the performance is less explored. In the model system of the Si-based photoanode paired with different transition-metal-based EC dual layers, the oxygen evolution reaction with high efficiency and stability is obtained at low cost via synergetic effects of dual ECs. The spontaneous mutual doping between the EC dual layers greatly increases the conductivity of the electrode, thus facilitating the interfacial charge transfer, and the EC interlayer with high hole-accumulation ability can dramatically improve the hole collection capacity of the EC overlayer. In addition, the dynamic cycle of dissolution, diffusion, and deposition of a tiny amount of metal species between the EC dual layers favors the electrode stability. This work provides insightful guidance to interface design of high-performance devices for solar energy conversion.

**KEYWORDS:** oxygen evolution reaction, Si-based photoanode, interfacial engineering, self-reconstruction, artificial photosynthesis, spontaneous mutual doping, transition-metal electrocatalyst



## 1. INTRODUCTION

Solar water splitting is promising for conversion of solar energy into emission-free renewable and clean hydrogen fuel, while it is a great challenge to develop a high-efficiency, economical, and stable water-splitting system.<sup>1–5</sup> Integration of electrocatalysts (ECs) with photoabsorbers is indispensable for high-performance solar water-splitting devices because they can minimize the kinetic overpotential losses associated with the water-splitting reaction,<sup>6</sup> passivate semiconductor surface states responsible for Fermi-level pinning,<sup>7</sup> improve charge transfer,<sup>8</sup> increase the photovoltage,<sup>8–10</sup> or function as a physical barrier to protect photoabsorbers.<sup>6,8–16</sup> Most studies are focused on the roles of each single EC, while how the interaction between different ECs affects the performance is less explored. Taking the Si-based photoanode paired with two different transition-metal-based EC layers as a model system, we investigate the effect of the interaction between EC layers on the photoelectrochemical (PEC) oxygen evolution reaction (OER) by systematically varying the metal species (Fe, Co, or Ni) in both the interlayer and overlayer ECs. Technologically well-developed Si is chosen as the photoabsorber because of its excellent light absorption with a suitable bandgap of ~1.12 eV, high carrier mobility, and superabundance.<sup>17</sup> The first-row 3d-transition-metal (Fe, Co, and Ni) based ECs hold great

potential to replace noble metals for large-scale practical applications owing to their high efficiency,<sup>10</sup> low cost,<sup>10,14,18–20</sup> and negligible contact resistance with Si.<sup>8,10,21</sup>

The spontaneous mutual doping between the two EC layers greatly increases the conductivity of the electrode, thus facilitating the interfacial charge transfer,<sup>22–28</sup> and the EC interlayer with high hole-accumulation capacity can dramatically improve the hole-collection capacity of the EC overlayer. In addition, the dynamic cycle of dissolution, diffusion, and deposition of a tiny amount of metal species between the two EC layers favors the photoanode stability. As a result, our best Si-based anode with the partially activated Ni interlayer and FeOOH overlayer obtains excellent OER performance at low cost.

## 2. RESULTS AND DISCUSSION

The procedure of fabricating the n<sup>+</sup>p-Si/SiO<sub>x</sub>/aNi:FeOOH (aNi = Ni/NiO<sub>x</sub>H<sub>y</sub>) photoanode is depicted in Figure 1a. First, the Ni metal layer was thermally deposited on the p-side surface of n<sup>+</sup>p-Si with a native SiO<sub>x</sub> layer. Then, cyclic

Received: June 17, 2019

Accepted: September 13, 2019

Published: September 13, 2019

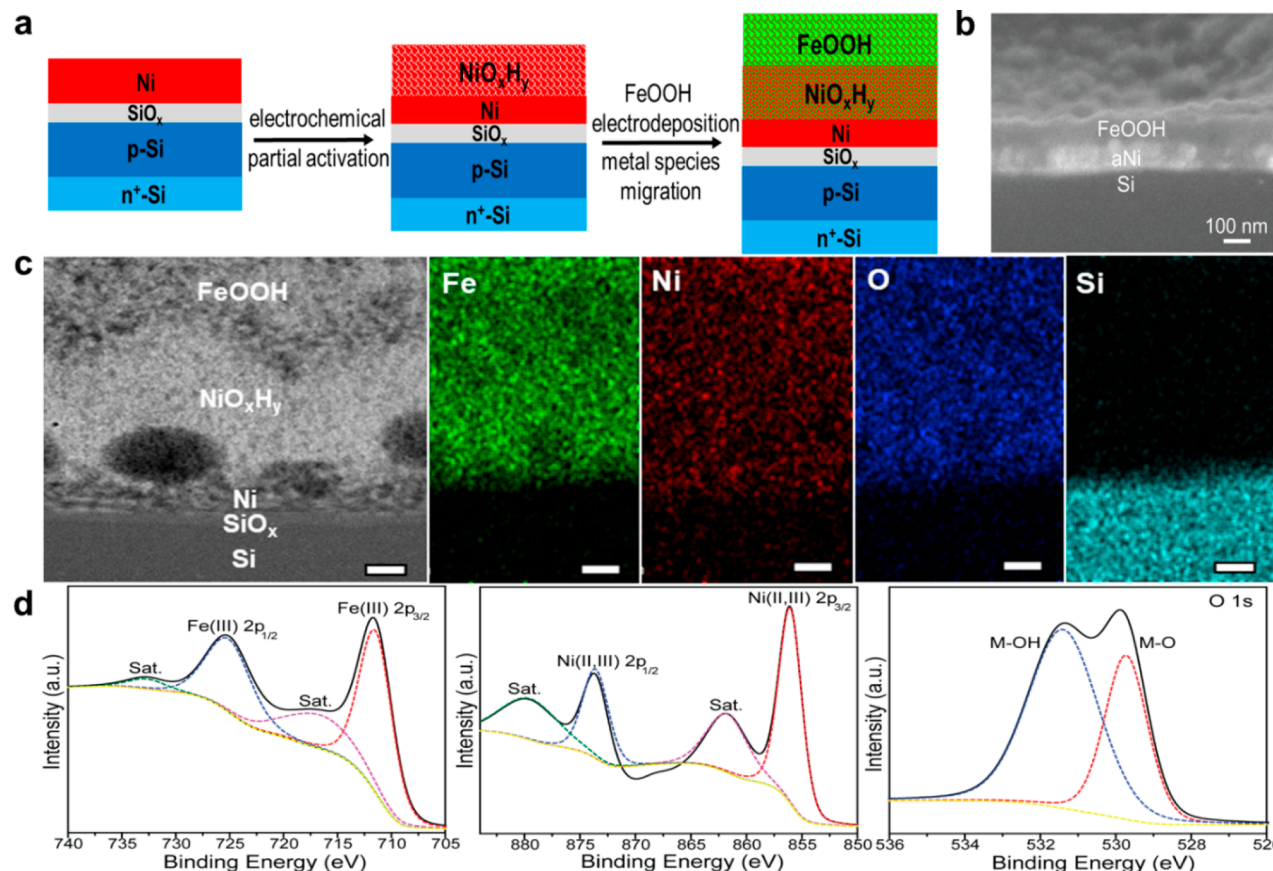


**Figure 1.** (a) Schematic fabrication procedure and (b) cross-sectional SEM image and (c) high-resolution cross-sectional TEM image and corresponding EDS elemental mapping images (scale bars: 50 nm) and XPS spectra of Fe 2p, Ni 2p, and O 1s (d) of the n<sup>+</sup>p-Si/SiO<sub>x</sub>/aNi:FeOOH photoanode.

voltammogram (CV) cycles were performed to electrochemically activate the partial Ni to NiO<sub>x</sub>H<sub>y</sub>, which expands the volume of the Ni layer and prevents further oxidation of Ni.<sup>8,29</sup> Finally, the FeOOH overlayer was electrodeposited onto the NiO<sub>x</sub>H<sub>y</sub> surface (see the experimental details in the Supporting Information). The two EC layers (FeOOH and aNi) on the Si surface with the similar thickness of ~100 nm, intimate contact, and different contrast are displayed from the cross-sectional scanning electron microscopy (SEM) image (Figure 1b). The spherical aberration-corrected high-resolution transmission electron microscopy (Cs-corrected HRTEM) image also distinguishes the NiO<sub>x</sub>H<sub>y</sub>, Ni, and SiO<sub>x</sub> layers.<sup>8</sup> Interestingly, the corresponding energy-dispersive X-ray spectroscopy (EDS) elemental mapping images disclose a relatively uniform distribution of Fe, Ni, and O over Si, indicating that the Ni element incorporates into the FeOOH overlayer and the Fe element into the NiO<sub>x</sub>H<sub>y</sub> interlayer since migration of the metal species within the transition metal oxy(hydroxide) layer occurs readily during the electrochemical cycling at the last fabrication step (Figure 1c, Figures S1–S3).<sup>30</sup> The surface chemical states of Fe, Ni, and O elements in n<sup>+</sup>p-Si/SiO<sub>x</sub>/aNi:FeOOH are analyzed by X-ray photoelectron spectroscopy (XPS) (Figure S4, Figure 1d, and Table S1). For the Fe 2p spectrum, two core-level peaks of Fe 2p<sub>3/2</sub> at 711.6 eV and Fe 2p<sub>1/2</sub> at 725.2 eV are present, implying the existence of FeOOH with the Fe<sup>3+</sup> oxidation state.<sup>31</sup> The XRD and Raman spectra analyses of the crystallinity and composition of the anode surface layer also confirm the existence of FeOOH (Figure S5). The peak centered at ~855.9 eV with an

associated satellite peak at ~861.8 eV can be assigned to Ni 2p<sub>3/2</sub> of the NiO<sub>x</sub>H<sub>y</sub> (either Ni(OH)<sub>2</sub> or NiOOH) phase.<sup>8,30,32</sup> This result corroborates that the Ni ions in the interlayer dissolve, diffuse, and deposit on the overlayer during the FeOOH electrochemical deposition process since the Ni signal from the aNi interlayer cannot be probed by XPS through the ~100 nm thick and relatively dense FeOOH overlayer due to the limited XPS detection depth.<sup>30,33,34</sup> In the O 1s region of XPS, there are two major peaks at 529.1 eV and 531.3 corresponding to metal–oxide (M–O) and metal–hydroxyl (M–OH) binding energies, respectively.<sup>35,36</sup> The ratio of the O<sup>2–</sup> and OH<sup>–</sup> peak areas is estimated to be 1.03, which is close to the theoretical ratio of 1:1 between O<sup>2–</sup> and OH<sup>–</sup> in the metal oxyhydroxide MOOH.<sup>37</sup> In our case, it is Ni(Fe)O<sub>x</sub>H<sub>y</sub>, representing Ni-doped FeOOH in the overlayer and/or Fe-doped NiO<sub>x</sub>H<sub>y</sub> in the interlayer. For clarity, we use aNi:FeOOH to denote the mutual doping between the two EC layers, and the partial charge transfer from Ni to Fe sites will enhance the OER activity.<sup>38,39</sup>

Besides n<sup>+</sup>p-Si/SiO<sub>x</sub>/aNi:FeOOH, the n<sup>+</sup>p-Si/SiO<sub>x</sub>/aM:FeOOH (aM = M/MO<sub>x</sub>H<sub>y</sub>, M = Fe, Co) photoanodes were also fabricated for comparison following the similar fabrication procedure except replacing the interlayer Ni species with Fe and Co (Figure S6). The PEC performances of the n<sup>+</sup>p-Si/SiO<sub>x</sub>/aM (M = Fe, Co, Ni) photoanodes with and without the FeOOH overlayer were evaluated using a three-electrode CV configuration in 1.0 M KOH solution under simulated AM 1.5G back irradiation at 1 sun (Figure 2) after optimizing the thicknesses of the two EC layers (Figure S7, Tables S2–S5,

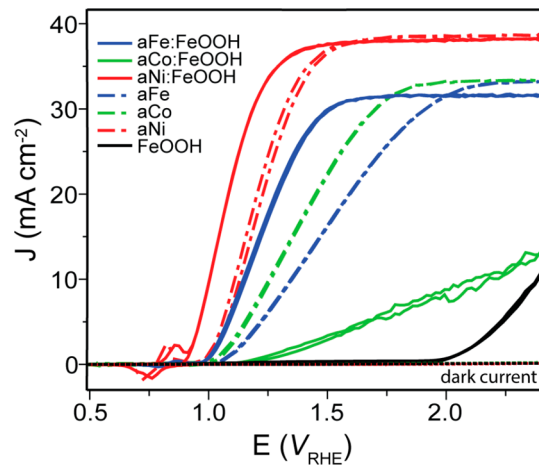


**Figure 2.** PEC performance of photoanodes.  $J$ – $V$  behavior in 1 M KOH electrolyte at the scan rate of 50  $\text{mV s}^{-1}$  under irradiation of 100  $\text{mW cm}^{-2}$  (AM 1.5G).

and Figure S8). To avoid the trade-off between light absorption and catalytic activity at various EC film thicknesses, the back-side illumination configuration was adopted in our work, which has the advantage of spatially and functionally decoupling the light absorption and the catalytic activity.<sup>8,21,40</sup> The PEC activity of  $n^+p\text{-Si}/\text{SiO}_x/\text{aM}$  is in the order of  $n^+p\text{-Si}/\text{SiO}_x/\text{aNi} > n^+p\text{-Si}/\text{SiO}_x/\text{aCo} > n^+p\text{-Si}/\text{SiO}_x/\text{aFe}$ . Except  $n^+p\text{-Si}/\text{SiO}_x/\text{aCo}$ , the activities of both  $n^+p\text{-Si}/\text{SiO}_x/\text{aNi}$  and  $n^+p\text{-Si}/\text{SiO}_x/\text{aFe}$  enhance after coating FeOOH. All photoanodes are listed in the order of descending activity by comparing the photocurrent at 1.23 V versus reversible hydrogen electrode ( $V_{\text{RHE}}$ ) as shown in Table 1.

The  $n^+p\text{-Si}/\text{SiO}_x/\text{aNi:FeOOH}$  photoanode has the highest activity among all photoanodes, offering a typical photocurrent onset potential of  $\sim 0.91 \text{ V}_{\text{RHE}}$ , a photocurrent density of  $\sim 33.2 \text{ mA cm}^{-2}$  at 1.23  $V_{\text{RHE}}$ , and a saturation current density of  $\sim 38.5 \text{ mA cm}^{-2}$  (Figure 2), which is 88.1% of the theoretical value ( $43.7 \text{ mA cm}^{-2}$ ) that crystalline Si can afford.<sup>8</sup> The dark currents of all the anodes are near zero, implying that the observed current under irradiation is exclusively related to the photogenerated charge carriers. Based on the 100% Faradaic efficiency (Figure S9a), the applied bias photon-to-current efficiency (ABPE, also called the ideal solar-to-O<sub>2</sub> conversion efficiency) of this photoelectrode is calculated to be 3.4% at 0.95  $V_{\text{RHE}}$  (Figure S9b). This PEC-OER performance is excellent compared to the reported Si-based photoanodes (Table S6).

To explore the underlying mechanism for the excellent OER performance of  $n^+p\text{-Si}/\text{SiO}_x/\text{aNi:FeOOH}$  compared to other photoanodes, both thermodynamics (photovoltage) and

kinetics (surface active sites, surface catalytic kinetics, and interfacial charge transfer) aspects were investigated. We first tested the photovoltages of the  $n^+p\text{-Si}/\text{SiO}_x/\text{aM}$  ( $\text{M} = \text{Fe}, \text{Co}, \text{Ni}$ ) photoanodes with and without the FeOOH overlayer via the potential difference between the photoanodes under irradiation and a metallic (heavily doped)  $p^{+2}\text{-Si}$  (0.001 to 0.005  $\Omega \text{ cm}^{-1}$ ) coated with the same EC layer in the dark (Figure S10).

The photovoltage comparison (Figure 3a) shows that the changing trend in the photovoltage with and without the FeOOH overlayer is inconsistent with that in the OER activity (Table 1). Electrochemically active surface area (ECSA) measurements are estimated from electrochemical double-layer capacitance ( $C_{\text{dl}}$ ) in a CV potential range when a non-Faradaic process occurs,<sup>40</sup> which represents the EC porosity property to some extent, showing that the changing trend in the ECSA of  $n^+p\text{-Si}/\text{SiO}_x/\text{aM}$  ( $\text{M} = \text{Fe}, \text{Co}, \text{Ni}$ ) with and without the FeOOH overlayer is also in agreement with that in the OER activity of these anodes (Figure 3b, Table 1). In our work, the highest ECSA (0.513  $\text{mF cm}^{-2}$ ) is obtained for the FeOOH overlayer deposition on  $n^+p\text{-Si}/\text{SiO}_x/\text{aNi}$ , which is 6.4-fold as large as that in  $n^+p\text{-Si}/\text{SiO}_x/\text{aNi}$  (0.08  $\text{mF cm}^{-2}$ ) (Figure 3b). The changing trend of the EC activity (Figure S10) is consistent with that of PEC activity (Figures 2 and S10) of  $n^+p\text{-Si}/\text{SiO}_x/\text{aM}$  ( $\text{M} = \text{Fe}, \text{Co}, \text{Ni}$ ) anodes with and without FeOOH, which is further proved by Tafel plot measurements (Figure S11) estimated from  $J$ – $V$  curves (Figure 2, Table 1). Furthermore, the interfacial charge transfer behaviors of these photoanodes were investigated by electrochemical impedance spectroscopy (EIS) (Figure 3c, Figure S12, and Table S7). The EIS data show that the changing trend in the interfacial resistance of the  $n^+p\text{-Si}/\text{SiO}_x/\text{aM}$  ( $\text{M} = \text{Fe}, \text{Co}, \text{Ni}$ ) photoanodes both with and without the FeOOH overlayer is in agreement with that in the OER activity; that is, smaller interfacial resistance corresponds to higher OER performance (Table 1). It is consistent with previous reports that a small amount of transition metal can dissolve into other transition metal oxy(hydroxide)s, which will enhance the electrical conductivity of metal oxy(hydroxide) and promote the formation of metal ions with high oxidation states as active sites to facilitate reactions with OH<sup>−</sup> to evolve O<sub>2</sub>.<sup>22–28</sup> As summarized in Table 1, the decrease in the OER activity of the  $n^+p\text{-Si}/\text{SiO}_x/\text{aM}$  ( $\text{M} = \text{Fe}, \text{Co}, \text{Ni}$ ) photoanodes both with and without the FeOOH overlayer is consistent with increasing interfacial charge transfer resistance, which hinders the transfer of photogenerated holes to the electrode surface, while it is not directly associated with variation in photovoltage or surface active sites.

Since transition-metal-based ECs have relatively large charge storage ability,<sup>41</sup> we further explored its effect on the OER

**Table 1. Comparison of Changing Trend in Photocurrent Density, Photovoltage, ECSA, Tafel Slope, and Interfacial Resistance for  $n^+p\text{-Si}/\text{SiO}_x/\text{aM}$  ( $\text{M} = \text{Fe}, \text{Co}, \text{Ni}$ ) Anodes with and without the FeOOH Overlayer in the Order of Descending OER Activity**

photoanode	photocurrent density at 1.23 $V_{\text{RHE}}$	photovoltage (mV <sub>RHE</sub> )	ECSA ( $\text{mF cm}^{-2}$ )	Tafel slope ( $\text{mV dec}^{-1}$ )	interfacial resistance ( $\Omega$ )
aNi:FeOOH	33.20	610	0.513	46	2.60
aNi	22.32	530	0.080	68	4.93
aFe:FeOOH	16.15	600	0.202	92	7.19
aCo	9.60	590	0.275	114	11.06
aFe	5.63	590	0.047	119	14.29
aCo:FeOOH	0.79	530	0.091	270	308.37

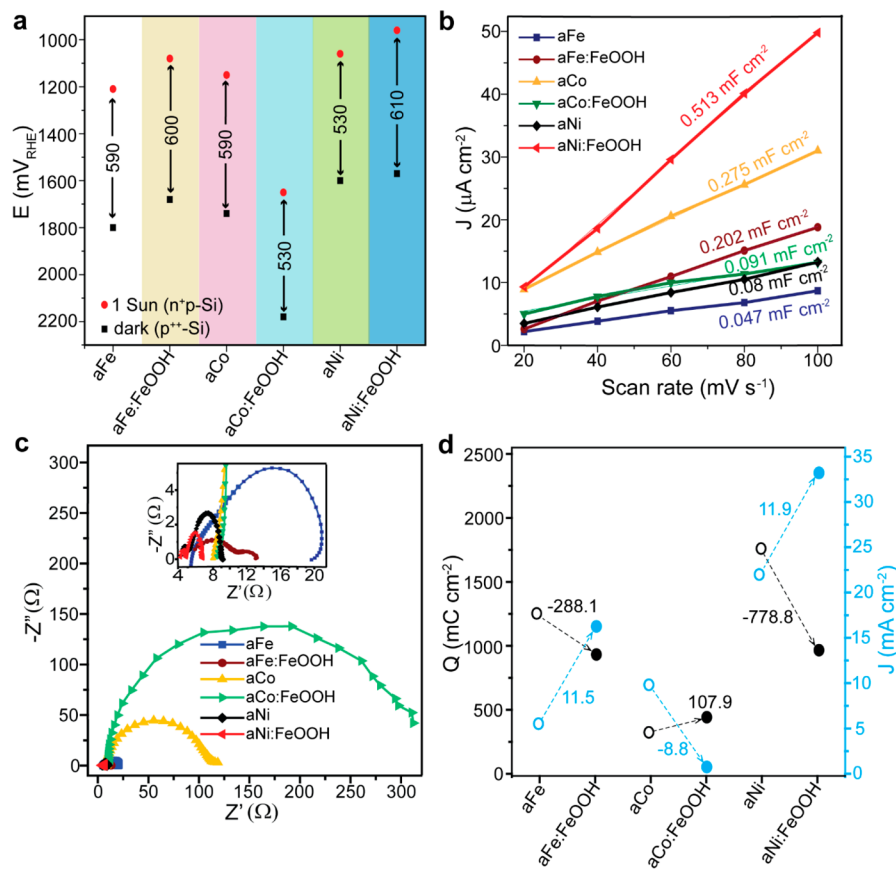


**Figure 3.** Comparison of (a) the photovoltage determined by the potential difference between the catalyst layer coated on n<sup>+</sup>p-Si/SiO<sub>x</sub> under irradiation and on metallic p<sup>++</sup>-Si/SiO<sub>x</sub> in the dark at 5 mA cm<sup>-2</sup> in mV<sub>RHE</sub> (mV versus RHE), (b) Capacitive currents at different scan rates (the linear slope, equivalent to twice the double-layer capacitance C<sub>db</sub>, is used to represent the ECSA), (c) impedance Nyquist plots measured at 1.23 V<sub>RHE</sub> under 1 sun irradiation (inset shows the zoomed-in high-frequency part), and (d) relationship between the surface hole-accumulation capacity (Q) and the photocurrent density (J) for the n<sup>+</sup>p-Si/SiO<sub>x</sub>/aM (M = Fe, Co, Ni) photoanodes with and without the FeOOH overlayer.

activity by the chopped light chronoamperometric hole-accumulation measurements. To evaluate the hole-accumulation ability of the n<sup>+</sup>p-Si/SiO<sub>x</sub>/aM (M = Fe, Co, Ni) photoanodes with and without the FeOOH overlayer, we used a transient photocurrent surface charging–discharging method to test the density of the accumulated holes under steady-state conditions during the OER at 1.23 V<sub>RHE</sub> (Figure S13). The close relationship between the interlayer hole-accumulation/ the overlayer hole-collection capacity and the OER activity of the photoanodes was summarized in Figure 3d. This result shows that the n<sup>+</sup>p-Si/SiO<sub>x</sub>/aNi electrode surface exhibits the highest hole-accumulation capacity among n<sup>+</sup>p-Si/SiO<sub>x</sub>/aM (M = Fe, Co, Ni), indicating the lowest charge recombination at the interface. After depositing FeOOH, FeOOH can efficiently collect the maximum photogenerated holes from the activated Ni metal interlayer for the OER, as indicated by the simultaneous biggest decrease in surface hole accumulation (Q) and biggest increase in photocurrent density (J) from n<sup>+</sup>p-Si/SiO<sub>x</sub>/aNi to n<sup>+</sup>p-Si/SiO<sub>x</sub>/aNi:FeOOH. Both a decrease in Q and increase in J from n<sup>+</sup>p-Si/SiO<sub>x</sub>/aFe to n<sup>+</sup>p-Si/SiO<sub>x</sub>/aFe:FeOOH are second to the Ni counterpart. In contrast, FeOOH cannot efficiently collect the photogenerated holes from the activated Co metal interlayer for the OER as shown by the increase in Q and decrease in J. It is noted that the increase in the amount of both the injected holes for the OER and the accumulated surface holes leads to the higher photocurrent in n<sup>+</sup>p-Si/SiO<sub>x</sub>/aM:FeOOH (M = Fe, Co, Ni),

implying that surface charge concentration and interfacial charge transfer behavior are central to water-splitting performance.<sup>42</sup>

Apart from the activity, the durability of a photoelectrode is also crucial for its commercial application, so we evaluated the stability of the representative n<sup>+</sup>p-Si/SiO<sub>x</sub>/aNi:FeOOH photoanode by continuous chronoamperometric operation in 1.0 M KOH solution carried out at 1.0 V<sub>RHE</sub>. After a 110 h test, the photoanode shows little change in the photocurrent density (Figure 4a), chemical structure (Figures S4 and S5), and morphology (Figure S14). The current fluctuation in Figure 4a was caused by the absorption/desorption of O<sub>2</sub> bubbles and

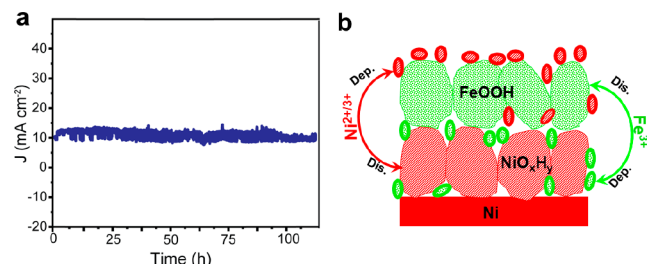


**Figure 4.** Photocurrent as a function of time (J–t) for the n<sup>+</sup>p-Si/SiO<sub>x</sub>/aNi:FeOOH photoanode (a) and metal species dissolution, diffusion, and deposition cycle between the aNi interlayer and the FeOOH overlayer (b).

fluctuations in the irradiation intensity. The inductively coupled plasma-atomic emission spectroscopy (ICP-AES) shows that the original electrolyte is free of Ni and Fe metal ions. It indicates that the  $\text{NiO}_x\text{H}_y$  activation layer on the Ni underlayer works as the source for dissolved  $\text{Ni}^{2+/3+}$  ions since it is slightly soluble in 1.0 M KOH solution.<sup>29</sup> The dissolved  $\text{Ni}^{2+/3+}$  ions can easily diffuse around in the electrode due to the ion-permeable property of both  $\text{NiO}_x\text{H}_y$  and  $\text{FeOOH}$ <sup>15,43,44</sup> and recombine with hydroxide anions  $\text{OH}^-$  from the electrolyte to form  $\text{NiO}_x\text{H}_y$  on the surface of  $\text{FeOOH}$ . Similarly,  $\text{Fe}^{3+}$  ions will incorporate into  $\text{NiO}_x\text{H}_y$ . Both the doped EC overlayer and interlayer can be denoted as  $\text{Ni}(\text{Fe})\text{O}_x\text{H}_y$  (Figures 1c and 4b).<sup>29</sup> After the stability test, the ratio of Ni:Fe on the surface of the photoanode increases from 8:92 (before the stability test) to 19:81 (Figure S4), and the Ni and Fe metal ion concentration is measured to be very low (less than 0.1  $\mu\text{M}$ ). It further confirms the mutual doping of Ni and Fe metal ions between the two EC layers, and such a small metal consumption will not impact the electrical conductivity and mechanical strength of the photoanode and thus the OER performance.<sup>26,29,35,45–50</sup>

During long-term operation, *in situ* regeneration of aNi:FeOOH using dissolved Ni and Fe species might take place where the loss of water oxidation activity occurs due to catalyst dissolution or exfoliation, so the OER performance maintains. It is the beauty of self-doping from adjacent materials at low concentration since higher ion concentration will cause the photocurrent decline due to catalyst overloading.<sup>29</sup> So, we also assessed the OER activity of  $n^+p$ -Si/ $\text{SiO}_x/a\text{Ni:MOOH}$  ( $M = \text{Fe, Co, Ni}$ ) with different overlayers. The activity of these anodes at 1.23  $V_{\text{RHE}}$  is in the order of  $n^+p$ -Si/ $\text{SiO}_x/a\text{Ni:FeOOH} > n^+p$ -Si/ $\text{SiO}_x/a\text{Ni:NiOOH} > n^+p$ -Si/ $\text{SiO}_x/a\text{Ni:CoOOH}$  (Figure S15a and Table S8). The only difference in these anodes is the overlayer EC, but the activity of the EC film is in the order of  $\text{NiOOH} > \text{CoOOH} > \text{FeOOH}$ ,<sup>51</sup> which is inconsistent with the activity order of  $n^+p$ -Si/ $\text{SiO}_x/a\text{Ni:MOOH}$  ( $M = \text{Fe, Co, Ni}$ ), further proving the mutual doping effect between the interlayer and the overlayer ECs. Besides, as a metal ion source, the partially activated metal interlayer has chemical composition and is structurally similar to the overlayer EC and excellent contact with Si, which favors the stability of the electrode. Without the interlayer, the activity of the controlled sample  $n^+p$ -Si/ $\text{SiO}_x/(\text{Ni}_{0.33}\text{Fe}_{0.66})\text{-OOH}$  degrades rapidly (Figure S16), similar to the previous report.<sup>8</sup> In addition, the variation trend in activity for  $n^+p$ -Si/ $\text{SiO}_x/a\text{Ni:MOOH}$  ( $M = \text{Fe, Co, Ni}$ ) is consistent with that of the interfacial charge transfer resistance (Figure S15b) and has no close relation with photovoltage (Figure S15c) or surface active sites (Figure S15d and Table S8), which demonstrates the generality of mutual doping between transition-metal-based ECs.

### 3. CONCLUSION

In summary, the Si-based photoanode decorated with transition-metal-based EC dual layers affords the excellent water oxidation performance with high efficiency and stability at low cost via synergetic effects of dual ECs. The spontaneous mutual doping between the EC dual layers greatly increases the conductivity of the electrode, thus facilitating the interfacial charge transfer, and the EC interlayer with higher hole-accumulation ability can dramatically improve the hole-collection capacity of the EC overlayer. In addition, the dynamic cycle of dissolution, diffusion, and deposition of a tiny

amount of metal species between the EC dual layers favors the photoanode stability. This work provides insightful guidance to interface design of high-performance devices for solar energy conversion.

### ■ ASSOCIATED CONTENT

#### S Supporting Information

The Supporting Information is available free of charge on the ACS Publications website at DOI: 10.1021/acsael.9b01209.

Experimental details, fabrication of photoanodes, characterizations, PEC measurements, SEM images, XRD pattern, Raman spectra, XPS survey spectra, electrochemical measurements,  $J-V$  curves, Faradaic efficiency, applied bias photon-to-current efficiency, electrochemical impedance spectroscopy, Tafel, ECSA, photovoltage, and Si-based photoanode materials comparison list (PDF)

### ■ AUTHOR INFORMATION

#### Corresponding Author

\*E-mail: gongjr@nanoctr.cn.

#### ORCID

Jian Ru Gong: 0000-0003-1512-4762

#### Author Contributions

<sup>†</sup>R.B., B.G., and A.A. contributed equally.

#### Notes

The authors declare no competing financial interest.

### ■ ACKNOWLEDGMENTS

This work was supported by the National Natural Science Foundation of China (21872043, 21422303, 21573049), National Key R&D Program “Nanotechnology” special focus (2016YFA0201600), Beijing Natural Science Foundation (2142036), the Knowledge Innovation Program and Youth Innovation Promotion Association, Special Program of “One Belt One Road” of CAS, and “CAS President’s International Fellowship Initiative”.

### ■ REFERENCES

- Lewis, N. S. Research Opportunities to Advance Solar Energy Utilization. *Science* **2016**, *351* (6271), No. aad1920.
- Kudo, A.; Miseki, Y. Heterogeneous Photocatalyst Materials for Water Splitting. *Chem. Soc. Rev.* **2009**, *38* (1), 253–278.
- Zhang, K.; Dong, T.; Xie, G.; Guan, L.; Guo, B.; Xiang, Q.; Dai, Y.; Tian, L.; Batool, A.; Jan, S. U.; Gong, J. R. Sacrificial Interlayer for Promoting Charge Transport in Hematite Photoanode. *ACS Appl. Mater. Interfaces* **2017**, *9* (49), 42723–42733.
- Guo, B.; Tian, L.; Xie, W.; Batool, A.; Xie, G.; Xiang, Q.; Jan, S. U.; Boddula, R.; Gong, J. R. Vertically Aligned Porous Organic Semiconductor Nanorod Array Photoanodes for Efficient Charge Utilization. *Nano Lett.* **2018**, *18* (9), 5954–5960.
- Walter, M. G.; Warren, E. L.; McKone, J. R.; Boettcher, S. W.; Mi, Q.; Santori, E. A.; Lewis, N. S. Solar Water Splitting Cells. *Chem. Rev.* **2010**, *110* (11), 6446–6473.
- Hill, J. C.; Landers, A. T.; Switzer, J. A. An Electrodeposited Inhomogeneous Metal-Insulator-Semiconductor Junction for Efficient Photoelectrochemical Water Oxidation. *Nat. Mater.* **2015**, *14* (11), 1150–1155.
- Thorne, J. E.; Jang, J.-W.; Liu, E. Y.; Wang, D. Understanding the Origin of Photoelectrode Performance Enhancement by Probing Surface Kinetics. *Chem. Sci.* **2016**, *7* (5), 3347–3354.
- Guo, B.; Batool, A.; Xie, G.; Boddula, R.; Tian, L.; Jan, S. U.; Gong, J. R. Facile Integration between Si and Catalyst for High-

- Performance Photoanodes by a Multifunctional Bridging Layer. *Nano Lett.* **2018**, *18* (2), 1516–1521.
- (9) Zhou, X.; Liu, R.; Sun, K.; Papadantonakis, K. M.; Brunschwig, B. S.; Lewis, N. S. 570 MV Photovoltage, Stabilized n-Si/CoO<sub>x</sub> Heterojunction Photoanodes Fabricated Using Atomic Layer Deposition. *Energy Environ. Sci.* **2016**, *9* (3), 892–897.
- (10) Yu, X.; Yang, P.; Chen, S.; Zhang, M.; Shi, G. NiFe Alloy Protected Silicon Photoanode for Efficient Water Splitting. *Adv. Energy Mater.* **2017**, *7* (6), 1601805.
- (11) Ji, L.; McDaniel, M. D.; Wang, S.; Posadas, A. B.; Li, X.; Huang, H.; Lee, J. C.; Demkov, A. A.; Bard, A. J.; Ekerdt, J. G.; Yu, E. T. A Silicon-Based Photocathode for Water Reduction with an Epitaxial SrTiO<sub>3</sub> protection Layer and a Nanostructured Catalyst. *Nat. Nanotechnol.* **2015**, *10* (1), 84–90.
- (12) Ji, L.; Hsu, H. Y.; Li, X.; Huang, K.; Zhang, Y.; Lee, J. C.; Bard, A. J.; Yu, E. T. Localized Dielectric Breakdown and Antireflection Coating in Metal-Oxide-Semiconductor Photoelectrodes. *Nat. Mater.* **2017**, *16* (1), 127–131.
- (13) Mei, B.; Seger, B.; Pedersen, T.; Malizia, M.; Hansen, O.; Chorkendorff, I.; Vesborg, P. C. K. Protection of p<sup>+</sup>-n-Si Photoanodes by Sputter-Deposited Ir/IrO<sub>x</sub> Thin Films. *J. Phys. Chem. Lett.* **2014**, *5* (11), 1948–1952.
- (14) Kenney, M. J.; Gong, M.; Li, Y.; Wu, J. Z.; Feng, J.; Lanza, M.; Dai, H. High-Performance Silicon Photoanodes Passivated with Ultrathin Nickel Films for Water Oxidation. *Science* **2013**, *342* (6160), 836–840.
- (15) Laskowski, F. A. L.; Nellist, M. R.; Qiu, J.; Boettcher, S. W. Metal Oxide/(Oxy)Hydroxide Overlays as Hole Collectors and Oxygen-Evolution Catalysts on Water-Splitting Photoanodes. *J. Am. Chem. Soc.* **2019**, *141* (4), 1394–1405.
- (16) Yang, J.; Cooper, J. K.; Toma, F. M.; Walczak, K. A.; Favaro, M.; Beeman, J. W.; Hess, L. H.; Wang, C.; Zhu, C.; Gul, S.; Yano, J.; Kisielowski, C.; Schwartzberg, A.; Sharp, I. D. A Multifunctional Biphasic Water Splitting Catalyst Tailored for Integration with High-Performance Semiconductor Photoanodes. *Nat. Mater.* **2017**, *16* (3), 335–341.
- (17) Sun, K.; Shen, S.; Liang, Y.; Burrows, P. E.; Mao, S. S.; Wang, D. Enabling Silicon for Solar-Fuel Production. *Chem. Rev.* **2014**, *114* (17), 8662–8719.
- (18) Oh, S.; Jung, S.; Lee, Y. H.; Song, J. T.; Kim, T. H.; Nandi, D. K.; Kim, S.-H.; Oh, J. Hole-Selective CoO<sub>x</sub>/SiO<sub>x</sub>/Si Heterojunctions for Photoelectrochemical Water Splitting. *ACS Catal.* **2018**, *8* (10), 9755–9764.
- (19) Zhao, J.; Gill, T. M.; Zheng, X. Enabling Silicon Photoanodes for Efficient Solar Water Splitting by Electroless-Deposited Nickel. *Nano Res.* **2018**, *11* (6), 3499–3508.
- (20) Li, C.; Huang, M.; Zhong, Y.; Zhang, L.; Xiao, Y.; Zhu, H. Highly Efficient NiFe Nanoparticle Decorated Si Photoanode for Photoelectrochemical Water Oxidation. *Chem. Mater.* **2019**, *31* (1), 171–178.
- (21) Bae, D.; Mei, B.; Frydendal, R.; Pedersen, T.; Seger, B.; Hansen, O.; Vesborg, P. C. K.; Chorkendorff, I. Back-Illuminated Si-Based Photoanode with Nickel Cobalt Oxide Catalytic Protection Layer. *ChemElectroChem* **2016**, *3* (10), 1517.
- (22) Lv, Y.; Batoool, A.; Wei, Y.; Xin, Q.; Boddula, R.; Jan, S. U.; Akram, M. Z.; Tian, L.; Guo, B.; Gong, J. R. Homogeneously Distributed NiFe Alloy Nanoparticles on 3D Carbon Fiber Network as a Bifunctional Electrocatalyst for Overall Water Splitting. *ChemElectroChem* **2019**, *6* (9), 2497–2502.
- (23) Shi, Y.; Yu, Y.; Liang, Y.; Du, Y.; Zhang, B. In Situ Electrochemical Conversion of an Ultrathin Tannin Nickel Iron Complex Film as an Efficient Oxygen Evolution Reaction Electrocatalyst. *Angew. Chem., Int. Ed.* **2019**, *58* (12), 3769–3773.
- (24) Corrigan, D. A. The Catalysis of the Oxygen Evolution Reaction by Iron Impurities in Thin Film Nickel Oxide Electrodes. *J. Electrochem. Soc.* **1987**, *134* (2), 377.
- (25) Trotochaud, L.; Young, S. L.; Ranney, J. K.; Boettcher, S. W. Nickel-Iron Oxyhydroxide Oxygen-Evolution Electrocatalysts: The Role of Intentional and Incidental Iron Incorporation. *J. Am. Chem. Soc.* **2014**, *136* (18), 6744–6753.
- (26) Görlin, M.; Chernev, P.; De Araújo, J. F.; Reier, T.; Dresp, S.; Paul, B.; Krähnert, R.; Dau, H.; Strasser, P. Oxygen Evolution Reaction Dynamics, Faradaic Charge Efficiency, and the Active Metal Redox States of Ni-Fe Oxide Water Splitting Electrocatalysts. *J. Am. Chem. Soc.* **2016**, *138* (17), 5603–5614.
- (27) Michael, J. D.; Demeter, E. L.; Illes, S. M.; Fan, Q.; Boes, J. R.; Kitchin, J. R. Alkaline Electrolyte and Fe Impurity Effects on the Performance and Active-Phase Structure of NiOOH Thin Films for OER Catalysis Applications. *J. Phys. Chem. C* **2015**, *119* (21), 11475–11481.
- (28) Morales, D. M.; Masa, J.; Andronescu, C.; Schuhmann, W. Promotional Effect of Fe Impurities in Graphene Precursors on the Activity of MnO<sub>x</sub>/Graphene Electrocatalysts for the Oxygen Evolution and Oxygen Reduction Reactions. *ChemElectroChem* **2017**, *4* (11), 2835–2841.
- (29) Kuang, Y.; Jia, Q.; Ma, G.; Hisatomi, T.; Minegishi, T.; Nishiyama, H.; Nakabayashi, M.; Shibata, N.; Yamada, T.; Kudo, A.; Domen, K. Ultrastable Low-Bias Water Splitting Photoanodes via Photocorrosion Inhibition and in Situ Catalyst Regeneration. *Nat. Energy* **2017**, *2* (1), 16191.
- (30) Klaus, S.; Cai, Y.; Louie, M. W.; Trotochaud, L.; Bell, A. T. Effects of Fe Electrolyte Impurities on Ni(OH)<sub>2</sub>/NiOOH Structure and Oxygen Evolution Activity. *J. Phys. Chem. C* **2015**, *119* (13), 7243–7254.
- (31) Cai, Q.; Hong, W.; Jian, C.; Li, J.; Liu, W. Impact of Silicon Resistivity on the Performance of Silicon Photoanode for Efficient Water Oxidation Reaction. *ACS Catal.* **2017**, *7* (5), 3277–3283.
- (32) Shih, Y.-J.; Huang, Y.-H.; Huang, C. P. Electrocatalytic Ammonia Oxidation over a Nickel Foam Electrode: Role of Ni(OH)<sub>2</sub>(s)-NiOOH(s) Nanocatalysts. *Electrochim. Acta* **2018**, *263*, 261–271.
- (33) Sun, K.; McDowell, M. T.; Nielander, A. C.; Hu, S.; Shaner, M. R.; Yang, F.; Brunschwig, B. S.; Lewis, N. S. Stable Solar-Driven Water Oxidation to O<sub>2</sub>(G) by Ni-Oxide-Coated Silicon Photoanodes. *J. Phys. Chem. Lett.* **2015**, *6* (4), 592–598.
- (34) Trotochaud, L.; Ranney, J. K.; Williams, K. N.; Boettcher, S. W. Solution-Cast Metal Oxide Thin Film Electrocatalysts for Oxygen Evolution. *J. Am. Chem. Soc.* **2012**, *134* (41), 17253–17261.
- (35) Zhou, H.; Yu, F.; Zhu, Q.; Sun, J.; Qin, F.; Yu, L.; Bao, J.; Yu, Y.; Chen, S.; Ren, Z. Water Splitting by Electrolysis at High Current Densities under 1.6 V. *Energy Environ. Sci.* **2018**, *11* (10), 2858–2864.
- (36) Cai, L.; Zhao, J.; Li, H.; Park, J.; Cho, I. S.; Han, H. S.; Zheng, X. One-Step Hydrothermal Deposition of Ni:FeOOH onto Photoanodes for Enhanced Water Oxidation. *ACS Energy Lett.* **2016**, *1* (3), 624–632.
- (37) Tang, D.; Mabayoje, O.; Lai, Y.; Liu, Y.; Mullins, C. B. In Situ Growth of Fe(Ni)OOH Catalyst on Stainless Steel for Water Oxidation. *Chemistry Select* **2017**, *2* (7), 2230–2234.
- (38) Mei, B.; Permyakova, A. a; Frydendal, R.; Bae, D.; Pedersen, T.; Malacrida, P.; Hansen, O.; Stephens, I. E. L.; Vesborg, P. C. K.; Seger, B.; Chorkendorff, I. B. Iron-Treated NiO as a Highly Transparent P<sub>□</sub>Type Protection Layer for Efficient Si-Based Photoanodes. *J. Phys. Chem. Lett.* **2014**, *5* (20), 3456–3461.
- (39) Bates, M. K.; Jia, Q.; Doan, H.; Liang, W.; Mukerjee, S. Charge-Transfer Effects in Ni-Fe and Ni-Fe-Co Mixed-Metal Oxides for the Alkaline Oxygen Evolution Reaction. *ACS Catal.* **2016**, *6* (1), 155–161.
- (40) Huang, G.; Fan, R.; Zhou, X.; Xu, Z.; Zhou, W.; Dong, W.; Shen, M. A porous Ni-O/Ni/Si photoanode for stable and efficient photoelectrochemical water splitting. *Chem. Commun.* **2019**, *55*, 377–380.
- (41) Cui, C.; Heggen, M.; Zabka, W.; Cui, W.; Osterwalder, J.; Probst, B.; Alberto, R. Atomically Dispersed Hybrid Nickel-Iridium Sites for Photoelectrocatalysis. *Nat. Commun.* **2017**, *8* (1), 1341.
- (42) Xie, G.; Guan, L.; Zhang, L.; Guo, B.; Batoool, A.; Xin, Q.; Boddula, R.; Jan, S. U.; Gong, J. R. Interaction-Dependent Interfacial

Charge-Transfer Behavior in Solar Water-Splitting Systems. *Nano Lett.* **2019**, *19* (2), 1234–1241.

(43) Lin, F.; Boettcher, S. W. Adaptive Semiconductor/Electrocatalyst Junctions in Water-Splitting Photoanodes. *Nat. Mater.* **2014**, *13* (1), 81–86.

(44) Lin, F.; Bachman, B. F.; Boettcher, S. W. Impact of Electrocatalyst Activity and Ion Permeability on Water-Splitting Photoanodes. *J. Phys. Chem. Lett.* **2015**, *6* (13), 2427–2433.

(45) Wu, Z.; Zou, Z.; Huang, J.; Gao, F. NiFe<sub>2</sub>O<sub>4</sub> Nanoparticles/NiFe Layered Double-Hydroxide Nanosheet Heterostructure Array for Efficient Overall Water Splitting at Large Current Densities. *ACS Appl. Mater. Interfaces* **2018**, *10* (31), 26283–26292.

(46) Shen, J.; Wang, M.; Zhao, L.; Jiang, J.; Liu, H.; Liu, J. Self-Supported Stainless Steel Nanocone Array Coated with a Layer of Ni-Fe Oxides/(Oxy)Hydroxides as a Highly Active and Robust Electrode for Water Oxidation. *ACS Appl. Mater. Interfaces* **2018**, *10* (10), 8786–8796.

(47) Xu, L.; Zhang, F.-T.; Chen, J.-H.; Fu, X.-Z.; Sun, R.; Wong, C.-P. Amorphous NiFe Nanotube Arrays Bifunctional Electrocatalysts for Efficient Electrochemical Overall Water Splitting. *ACS Appl. Energy Mater.* **2018**, *1* (3), 1210–1217.

(48) Stevens, M. B.; Trang, C. D. M.; Enman, L. J.; Deng, J.; Boettcher, S. W. Reactive Fe-Sites in Ni/Fe (Oxy)Hydroxide Are Responsible for Exceptional Oxygen Electrocatalysis Activity. *J. Am. Chem. Soc.* **2017**, *139* (33), 11361–11364.

(49) Klaus, S.; Louie, M. W.; Trotocaud, L.; Bell, A. T. Role of Catalyst Preparation on the Electrocatalytic Activity of Ni<sub>1-x</sub>Fe<sub>x</sub>OOH for the Oxygen Evolution Reaction. *J. Phys. Chem. C* **2015**, *119* (32), 18303–18316.

(50) Zou, X.; Liu, Y.; Li, G.-D.; Wu, Y.; Liu, D.-P.; Li, W.; Li, H.-W.; Wang, D.; Zhang, Y.; Zou, X. Ultrafast Formation of Amorphous Bimetallic Hydroxide Films on 3D Conductive Sulfide Nanoarrays for Large-Current-Density Oxygen Evolution Electrocatalysis. *Adv. Mater.* **2017**, *29* (22), 1700404.

(51) Subbaraman, R.; Tripkovic, D.; Chang, K.-C.; Strmcnik, D.; Paulikas, A. P.; Hirunsit, P.; Chan, M.; Greeley, J.; Stamenkovic, V.; Markovic, N. M. Trends in Activity for the Water Electrolyser Reactions on 3d M(Ni,Co,Fe,Mn) Hydr(Oxy)Oxide Catalysts. *Nat. Mater.* **2012**, *11* (6), 550–557.